

Supporting Information

A family of lanthanide complexes with a bis-tridentate nitronyl nitroxide radical: syntheses, structures and magnetic properties

Hao Miao,^a Fu-Xing Shen,^a Dong Shao,^a Le Shi,^a Hong-Qing Li,^a Hai-Yan Wei,^{*b} Bao-Lin Wang^{*c} and Xin-Yi Wang^{*a}

^a. State Key Laboratory of Coordination Chemistry, Collaborative Innovation Center of Advanced Microstructures, School of Chemistry and Chemical Engineering, Nanjing University, Nanjing, 210023, China. E-mail: wangxy66@nju.edu.cn.

^b. Jiangsu Key Laboratory of Biofunctional Materials, School of Chemistry and Materials Science, Nanjing Normal University, Nanjing, 210023, China. Email: weihaiyan@njnu.edu.cn.

^c. Jiangsu Key Laboratory for NSLSCS, School of Physical Science and Technology, Nanjing Normal University, Nanjing 210023, China. E-mail: blwang@njnu.edu.cn

1. X-ray crystallography and powder x-ray diffraction.....	5
Table S1. Selected bond lengths [Å] and angles [°] for complex 1_{Gd}	5
Table S2. Selected bond lengths [Å] and angles [°] for complex 2_{Tb}	5
Table S3. Selected bond lengths [Å] and angles [°] for complex 3_{Dy}	5
Table S4. Selected bond lengths [Å] and angles [°] for complex 4_{Ho}	5
Table S5. Selected bond lengths [Å] and angles [°] for complex 5_{Er}	5
Table S6. Selected bond lengths [Å] and angles [°] for complex 6_{Yb}	6
Table S7. Selected bond lengths [Å] and angles [°] for complex 7_{Gd}	6
Table S8. Selected bond lengths [Å] and angles [°] for complex 8_{Tb}	6
Table S9. Selected bond lengths [Å] and angles [°] for complex 9_{Dy}	6
Table S10. Selected bond lengths [Å] and angles [°] for complex 10_{Ho}	7
Table S11. Selected bond lengths [Å] and angles [°] for complex 11_{Er}	7
Table S12. Lanthanide geometry analysis by using the Shape software for 1_{Gd}-6_{Er}	7
Table S13. Lanthanide geometry analysis by using the Shape software for 7_{Gd}-11_{Er}	8
Fig. S1 X-ray powder diffraction pattern of complex 1_{Gd}	9
Fig. S2 X-ray powder diffraction pattern of complex 2_{Tb}	9
Fig. S3 X-ray powder diffraction pattern of complex 3_{Dy}	9
Fig. S4 X-ray powder diffraction pattern of complex 4_{Ho}	10
Fig. S5 X-ray powder diffraction pattern of complex 5_{Er}	10
Fig. S6 X-ray powder diffraction pattern of complex 6_{Yb}	10
Fig. S7 X-ray powder diffraction pattern of complex 7_{Gd}	11
Fig. S8 X-ray powder diffraction pattern of complex 8_{Tb}	11
Fig. S9 X-ray powder diffraction pattern of complex 9_{Dy}	11
Fig. S10 X-ray powder diffraction pattern of complex 10_{Ho}	12
Fig. S11 X-ray powder diffraction pattern of complex 11_{Er}	12
Fig. S12 Infrared spectrum of complex 1_{Gd} at room temperature.....	12
Fig. S13 Infrared spectrum of complex 2_{Tb} at room temperature.....	13
Fig. S14 Infrared spectrum of complex 3_{Dy} at room temperature.....	13
Fig. S15 Infrared spectrum of complex 4_{Ho} at room temperature.....	13
Fig. S16 Infrared spectrum of complex 5_{Er} at room temperature.....	14
Fig. S17 Infrared spectrum of complex 6_{Yb} at room temperature.....	14
Fig. S18 Infrared spectrum of complex 7_{Gd} at room temperature.....	14
Fig. S19 Infrared spectrum of complex 8_{Tb} at room temperature.....	15
Fig. S20 Infrared spectrum of complex 9_{Dy} at room temperature.	15
Fig. S21 Infrared spectrum of complex 10_{Ho} at room temperature.	15
Fig. S22 Infrared spectrum of complex 11_{Er} at room temperature.....	16
2. Magnetic Properties	16
Fig. S23 Field dependent magnetizations at 2 K for 1_{Gd}-6_{Yb}	16
Fig. S24 Field dependent magnetizations at 2 K for 7_{Gd}-11_{Er}	17
Table S14. Relaxation fitting parameters from the least-square fitting of the Cole-Cole plots of 6_{Yb} according to the generalized Debye model.....	17
Fig. S25 The real and imaginary components of ac magnetic susceptibility for 2_{Tb} at 2 K under zero applied external dc field (left) and a dc field of 1000 Oe (right).....	17
Fig. S26 The real and imaginary components of ac magnetic susceptibility for 3_{Dy} at 2 K under	

zero applied external dc field (left) and a dc field of 1000 Oe (right).....	18
Fig. S27 The real and imaginary components of ac magnetic susceptibility for 4_{H₀} at 2 K under zero applied external dc field (left) and a dc field of 1000 Oe (right).....	18
Fig. S28 The real and imaginary components of ac magnetic susceptibility for 5_{Er} at 2 K under zero applied external dc field (left) and a dc field of 1000 Oe (right).....	18
Fig. S29 The real and imaginary components of ac magnetic susceptibility for 8_{Tb} at 2 K under zero applied external dc field (left) and a dc field of 1000 Oe (right).....	19
Fig. S30 The real and imaginary components of ac magnetic susceptibility for 9_{Dy} at 2 K under zero applied external dc field (left) and a dc field of 1000 Oe (right).....	19
Fig. S31 The real and imaginary components of ac magnetic susceptibility for 10_{H₀} at 2 K under zero applied external dc field (left) and a dc field of 1000 Oe (right).....	19
Fig. S32 The real and imaginary components of ac magnetic susceptibility for 11_{Er} at 2 K under zero applied external dc field (left) and a dc field of 1000 Oe (right).....	20
3. Details for calculations.....	20
Fig. S33 Calculated model structures of individual Ln ^{III} (Tb ^{III} , Dy ^{III} , Ho ^{III} , Er ^{III} or Yb ^{III}) fragments; H atoms are omitted.	21
Table S15. Calculated energy levels (cm ⁻¹), g (g_x , g_y , g_z) tensors and m_J values of the lowest several spin-orbit states of individual Ln ^{III} fragment (Tb ^{III} , Dy ^{III} , Ho ^{III} , Er ^{III} or Yb ^{III}) for complexes 2_{Tb}–6_{Yb} and 8_{Tb}–11_{Er} using CASSCF/RASSI-SO with MOLCAS 8.2.....	22
Table S16. Wave functions with definite projection of the total moment $ m_J \rangle$ for the lowest two spin-orbit states of individual Ln ^{III} fragments (Tb ^{III} , Dy ^{III} , Ho ^{III} , Er ^{III} or Yb ^{III}) for complexes 2_{Tb}–6_{Yb} and 8_{Tb}–11_{Er} using CASSCF/RASSI-SO with MOLCAS 8.2.....	25
Fig. S34 Magnetization blocking barriers for individual Ln ^{III} fragments in 2_{Tb}–6_{Yb} and 8_{Tb}–11_{Er} . The thick black lines represent the spin-orbit states as a function of their magnetic moment along the magnetic axis. The green lines correspond to the diagonal matrix element of the transversal magnetic moment; the blue lines represent Orbach relaxation processes. The path shown by the red arrows represents the most probable path for magnetic relaxation in the corresponding compounds. The numbers at each arrow stand for the mean absolute value of the corresponding matrix element of transition magnetic moment.	27
Fig. S35 Labeled one type of J in complexes 1_{Gd}–6_{Yb}	28
Fig. S36 Labeled two types of J in complexes 7_{Gd}–11_{Er}	28
Table S17. Exchange energies (cm ⁻¹), energy difference between each exchange doublet $\Delta_{\text{tun}}(\text{cm}^{-1})$ and main values of the g_z for the lowest several exchange doublets of complexes 2_{Tb}–6_{Yb} and 8_{Tb}–11_{Er}	29
Fig. S37 Calculated orientations of the local main magnetic axes of the ground spin-orbit state on Ln ^{III} (Tb ^{III} , Dy ^{III} , Ho ^{III} , Er ^{III} or Yb ^{III}) ions of complexes 2_{Tb}–6_{Yb} and 8_{Tb}–11_{Er}	30

4. Reference	31
--------------------	----

1. X-ray crystallography and powder x-ray diffraction

Table S1. Selected bond lengths [Å] and angles [°] for complex **1_{Gd}**.

Gd(01)-O(1)	2.3843(12)	Gd(01)-O(8)	2.4073(12)
Gd(01)-O(3)	2.3895(12)	Gd(01)-N(5)	2.6068(15)
Gd(01)-O(4)	2.3949(12)	Gd(01)-N(3)	2.6448(15)
Gd(01)-O(5)	2.3955(12)	O(1)-N(1)	1.2983(18)
Gd(01)-O(6)	2.4395(12)	O(2)-N(2)	1.260(2)
Gd(01)-O(7)	2.3757(12)	N(1)-O(1)-Gd(01)	128.72(10)

Table S2. Selected bond lengths [Å] and angles [°] for complex **2_{Tb}**.

Tb(01)-O(6)	2.361(2)	Tb(01)-O(7)	2.432(3)
Tb(01)-O(4)	2.367(3)	Tb(01)-N(6)	2.595(3)
Tb(01)-O(2)	2.374(3)	Tb(01)-N(4)	2.642(3)
Tb(01)-O(3)	2.382(3)	O(1)-N(1)	1.261(4)
Tb(01)-O(8)	2.384(3)	O(2)-N(2)	1.294(4)
Tb(01)-O(5)	2.393(2)	N(2)-O(2)-Tb(01)	129.0(2)

Table S3. Selected bond lengths [Å] and angles [°] for complex **3_{Dy}**.

Dy(01)-O(7)	2.350(2)	Dy(01)-O(6)	2.430(3)
Dy(01)-O(2)	2.363(3)	Dy(01)-N(5)	2.591(3)
Dy(01)-O(3)	2.367(2)	Dy(01)-N(4)	2.626(3)
Dy(01)-O(4)	2.372(2)	N(1)-O(1)	1.265(4)
Dy(01)-O(5)	2.375(2)	O(2)-N(2)	1.308(4)
Dy(01)-O(8)	2.382(3)	N(2)-O(2)-Dy(01)	128.7(2)

Table S4. Selected bond lengths [Å] and angles [°] for complex **4_{Ho}**.

Ho(01)-O(4)	2.3360(18)	Ho(01)-O(5)	2.4199(19)
Ho(01)-O(8)	2.3569(18)	Ho(01)-N(6)	2.584(2)
Ho(01)-O(6)	2.3601(18)	Ho(01)-N(3)	2.617(2)
Ho(01)-O(7)	2.3608(18)	O(1)-N(1)	1.294(3)
Ho(01)-O(1)	2.361(2)	O(2)-N(2)	1.261(3)
Ho(01)-O(3)	2.3696(19)	N(1)-O(1)-Ho(01)	129.27(16)

Table S5. Selected bond lengths [Å] and angles [°] for complex **5_{Er}**.

Er(01)-O(6)	2.321(6)	Er(01)-O(8)	2.410(6)
Er(01)-O(2)	2.337(6)	Er(01)-N(6)	2.575(7)
Er(01)-O(4)	2.343(6)	Er(01)-N(4)	2.610(7)
Er(01)-O(3)	2.345(6)	O(1)-N(1)	1.267(11)
Er(01)-O(7)	2.351(6)	O(2)-N(2)	1.311(10)
Er(01)-O(5)	2.373(6)	N(2)-O(2)-Er(01)	129.3(5)

Table S6. Selected bond lengths [Å] and angles [°] for complex **6_{Yb}**.

Yb(01)-O(6)	2.291(3)	Yb(01)-O(5)	2.407(3)
Yb(01)-O(7)	2.306(2)	Yb(01)-N(6)	2.536(3)
Yb(01)-O(4)	2.306(2)	Yb(01)-N(4)	2.631(3)
Yb(01)-O(3)	2.328(3)	O(1)-N(1)	1.265(4)
Yb(01)-O(2)	2.342(2)	O(2)-N(2)	1.283(3)
Yb(01)-O(8)	2.349(3)	N(2)-O(2)-Yb(01)	131.12(19)

Table S7. Selected bond lengths [Å] and angles [°] for complex **7_{Gd}**.

Gd(01)-O(13)	2.373(3)	Gd(02)-O(4)	2.377(4)
Gd(01)-O(14)	2.373(3)	Gd(02)-O(5)	2.412(3)
Gd(01)-O(11)	2.379(4)	Gd(02)-O(7)	2.422(4)
Gd(01)-O(12)	2.379(3)	Gd(02)-O(1)	2.435(3)
Gd(01)-O(9)	2.418(3)	Gd(02)-O(6)	2.437(3)
Gd(01)-O(2)	2.421(3)	Gd(02)-N(5)	2.592(4)
Gd(01)-O(10)	2.438(4)	Gd(02)-N(3)	2.735(4)
Gd(01)-N(6)	2.627(4)	O(1)-N(1)	1.280(5)
Gd(01)-N(4)	2.741(4)	O(2)-N(2)	1.286(5)
Gd(02)-O(8)	2.352(3)	N(1)-O(1)-Gd(02)	132.3(3)
Gd(02)-O(3)	2.362(4)	N(2)-O(2)-Gd(01)	130.8(3)

Table S8. Selected bond lengths [Å] and angles [°] for complex **8_{Tb}**.

Tb(01)-O(3)	2.351(3)	Tb(02)-O(13)	2.355(3)
Tb(01)-O(6)	2.358(3)	Tb(02)-O(9)	2.396(3)
Tb(01)-O(4)	2.364(3)	Tb(02)-O(10)	2.411(3)
Tb(01)-O(5)	2.367(3)	Tb(02)-O(11)	2.414(3)
Tb(01)-O(7)	2.397(3)	Tb(02)-O(1)	2.421(3)
Tb(01)-O(2)	2.408(3)	Tb(02)-N(6)	2.582(4)
Tb(01)-O(8)	2.428(3)	Tb(02)-N(4)	2.722(3)
Tb(01)-N(5)	2.616(3)	O(1)-N(1)	1.279(4)
Tb(01)-N(3)	2.724(3)	O(2)-N(2)	1.284(4)
Tb(02)-O(12)	2.335(3)	N(1)-O(1)-Tb(02)	132.5(2)
Tb(02)-O(14)	2.348(4)	N(2)-O(2)-Tb(01)	131.0(2)

Table S9. Selected bond lengths [Å] and angles [°] for complex **9_{Dy}**.

Dy(01)-O(10)	2.3235(18)	Dy(02)-O(8)	2.3467(17)
Dy(01)-O(11)	2.3438(17)	Dy(02)-O(5)	2.3669(17)
Dy(01)-O(13)	2.3606(17)	Dy(02)-O(7)	2.3692(16)
Dy(01)-O(14)	2.3704(18)	Dy(02)-O(2)	2.4252(17)
Dy(01)-O(9)	2.3743(18)	Dy(02)-O(6)	2.4263(19)
Dy(01)-O(12)	2.4132(19)	Dy(02)-N(6)	2.596(2)
Dy(01)-O(1)	2.4155(17)	Dy(02)-N(4)	2.7101(19)

Dy(01)-N(5)	2.5601(19)	O(1)-N(1)	1.280(3)
Dy(01)-N(3)	2.6879(19)	O(2)-N(2)	1.282(3)
Dy(02)-O(4)	2.3340(17)	N(1)-O(1)-Dy(01)	133.09(14)
Dy(02)-O(3)	2.3367(17)	N(2)-O(2)-Dy(02)	130.56(14)

Table S10. Selected bond lengths [Å] and angles [°] for complex **10_{Ho}**.

Ho(01)-O(12)	2.330(5)	Ho(02)-O(3)	2.343(5)
Ho(01)-O(11)	2.340(5)	Ho(02)-O(7)	2.376(5)
Ho(01)-O(14)	2.343(5)	Ho(02)-O(8)	2.389(5)
Ho(01)-O(13)	2.344(5)	Ho(02)-O(6)	2.401(5)
Ho(01)-O(9)	2.380(5)	Ho(02)-O(2)	2.404(5)
Ho(01)-O(1)	2.400(5)	Ho(02)-N(5)	2.567(6)
Ho(01)-O(10)	2.419(5)	Ho(02)-N(3)	2.703(6)
Ho(01)-N(6)	2.601(6)	O(1)-N(1)	1.279(7)
Ho(01)-N(4)	2.710(5)	O(2)-N(2)	1.273(7)
Ho(02)-O(5)	2.312(5)	N(1)-O(1)-Ho(01)	131.2(4)
Ho(02)-O(4)	2.329(6)	N(2)-O(2)-Ho(00)	132.6(4)

Table S11. Selected bond lengths [Å] and angles [°] for complex **11_{Er}**.

Er(01)-O(14)	2.312(4)	Er(02)-O(7)	2.339(3)
Er(01)-O(13)	2.314(3)	Er(02)-O(3)	2.356(3)
Er(01)-O(12)	2.317(3)	Er(02)-O(8)	2.357(3)
Er(01)-O(10)	2.339(4)	Er(02)-O(6)	2.393(3)
Er(01)-O(11)	2.345(3)	Er(02)-O(1)	2.395(3)
Er(01)-O(2)	2.408(3)	Er(02)-N(6)	2.545(4)
Er(01)-O(9)	2.408(3)	Er(02)-N(3)	2.660(4)
Er(01)-N(5)	2.586(4)	N(1)-O(1)	1.278(5)
Er(01)-N(4)	2.681(4)	N(2)-O(2)	1.276(5)
Er(02)-O(4)	2.298(3)	N(1)-O(1)-Er(02)	133.1(3)
Er(02)-O(5)	2.313(3)	N(2)-O(2)-Er(01)	130.5(3)

Table S12. Lanthanide geometry analysis by using the Shape software for **1_{Gd}-6_{Er}**.

Complex Label	1_{Gd}	2_{Tb}	3_{Dy}	4_{Ho}	5_{Er}	6_{Yb}
EP-9	36.654	36.435	36.633	36.627	36.670	36.174
OPY-9	22.618	22.513	22.628	22.598	22.658	21.750
HBPY-9	16.985	16.945	17.165	17.202	17.322	20.037
JTC-9	16.232	16.078	16.161	16.091	15.941	16.641
JCCU-9	10.245	10.254	10.412	10.354	10.473	9.658
CCU-9	9.093	9.093	9.288	9.239	9.347	8.727
JCSAPR-9	1.648	1.633	1.550	1.528	1.490	1.195

CSAPR-9	0.803	0.801	0.735	0.728	0.712	0.416
JTCTPR-9	3.371	3.407	3.332	3.292	3.274	2.513
TCTPR-9	1.847	1.878	1.833	1.839	1.838	0.732
JTDIC-9	13.386	13.407	13.528	13.483	13.485	12.886
HH-9	10.037	9.956	10.081	10.053	10.080	12.510
MFF-9	0.849	0.853	0.784	0.822	0.723	1.153

Table S13. Lanthanide geometry analysis by using the Shape software for **7_{Gd}-11_{Er}**.

	7_{Gd1}	7_{Gd2}	8_{Tb1}	8_{Tb2}	9_{Dy1}	9_{Dy2}	10_{Ho1}	10_{Ho2}	11_{Er1}	11_{Er2}
EP-9	36.297	36.793	36.472	36.880	36.156	36.693	36.544	37.062	36.960	36.405
OPY-9	22.610	22.957	22.663	22.956	21.611	22.455	22.660	22.920	22.589	21.681
HBPY-9	16.394	17.995	16.490	18.187	19.319	17.438	16.692	18.432	17.589	19.450
JTC-9	16.856	16.568	16.996	16.582	16.508	16.225	17.024	16.585	16.137	16.569
JCCU-9	9.688	10.905	9.914	10.924	11.055	10.282	10.186	10.898	10.238	11.002
CCU-9	9.033	9.633	9.152	9.726	9.706	9.346	9.173	9.848	9.329	9.807
JCSAPR-9	1.938	1.562	1.888	1.523	1.446	1.588	1.814	1.465	1.516	1.392
CSAPR-9	1.105	0.656	1.062	0.635	0.601	0.786	1.017	0.607	0.739	0.565
JTCTPR-9	3.491	3.059	3.352	2.956	2.701	2.717	3.187	2.864	2.585	2.580
TCTPR-9	1.787	1.427	1.708	1.369	0.802	1.378	1.584	1.297	1.305	0.765
JTDIC-9	12.121	13.669	12.272	13.657	12.433	13.591	12.287	13.628	13.575	12.519
HH-9	10.457	11.003	10.627	11.147	12.074	10.870	10.765	11.328	10.858	12.184
MFF-9	1.163	0.766	1.133	0.778	0.885	0.913	1.023	0.773	0.887	0.906

Code	Label	Symmetry	Shape
1	EP-9	D9h	Enneagon
2	OPY-9	C8v	Octagonal pyramid
3	HBPY-9	D7h	Heptagonal bipyramid
4	JTC-9	C3v	Triangular cupola (J3) = trivacant cuboctahedron
5	JCCU-9	C4v	Capped cube (Elongated square pyramid, J8)
6	CCU-9	C4v	Capped cube
7	JCSAPR-9	C4v	Capped sq. antiprism (Gyroelongated square pyramid J10)
8	CSAPR-9	C4v	Capped square antiprism
9	JTCTPR-9	D3h	Tricapped trigonal prism (J51)
10	TCTPR-9	D3h	Tricapped trigonal prism
11	JTDIC-9	C3v	Tridiminished icosahedron (J63)
12	HH-9	C2v	Hula-hoop
13	MFF-9	Cs	Muffin

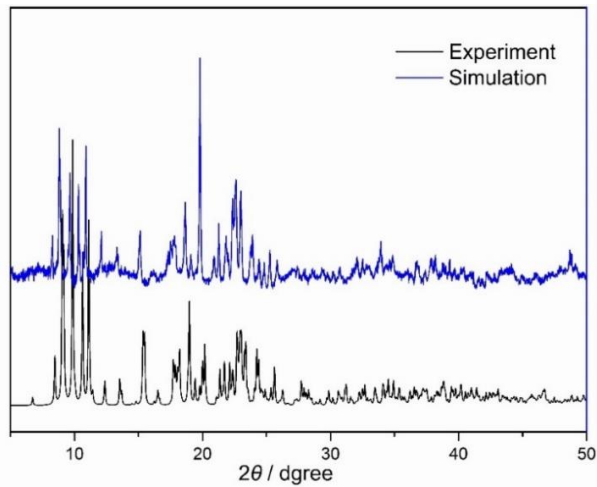


Fig. S1 X-ray powder diffraction pattern of complex **1_{Gd}**.

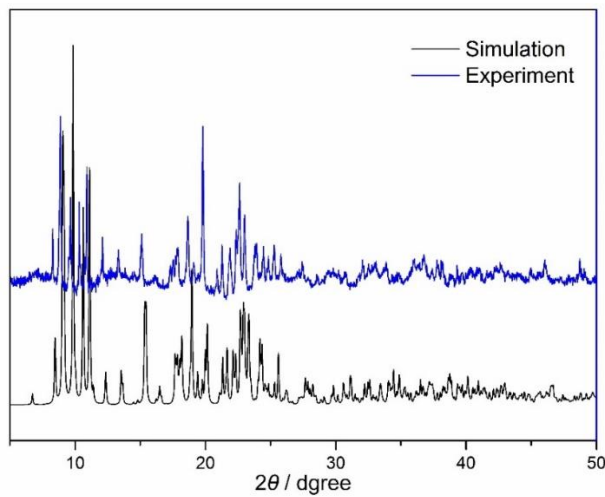


Fig. S2 X-ray powder diffraction pattern of complex **2_{Tb}**.

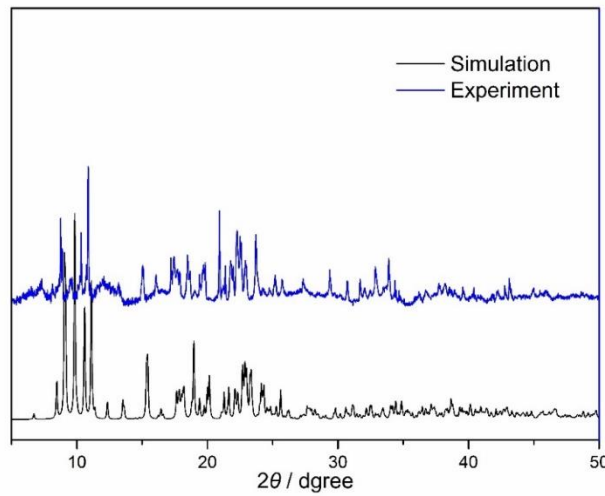


Fig. S3 X-ray powder diffraction pattern of complex **3_{Dy}**.

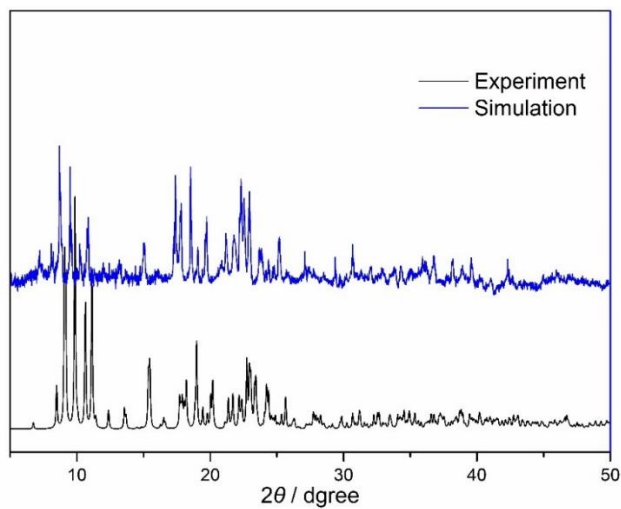


Fig. S4 X-ray powder diffraction pattern of complex $\mathbf{4}_{\text{Ho}}$.

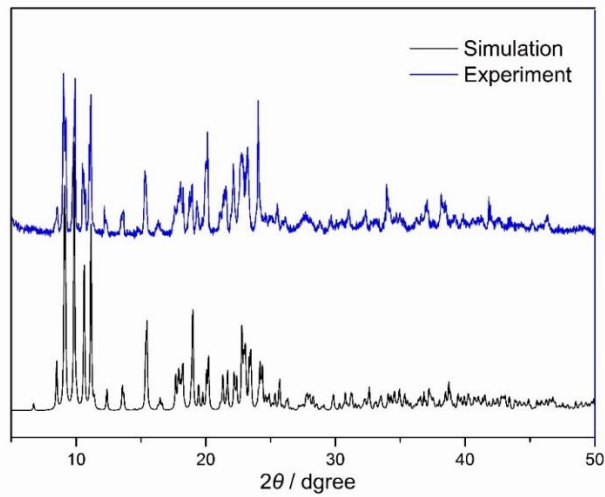


Fig. S5 X-ray powder diffraction pattern of complex $\mathbf{5}_{\text{Er}}$.

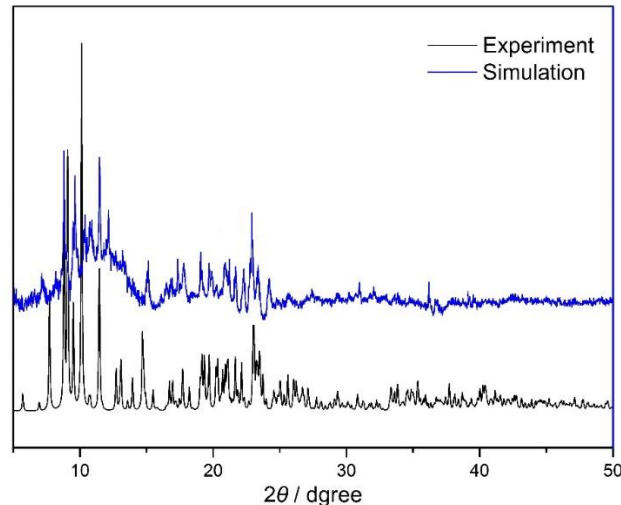


Fig. S6 X-ray powder diffraction pattern of complex $\mathbf{6}_{\text{Yb}}$.

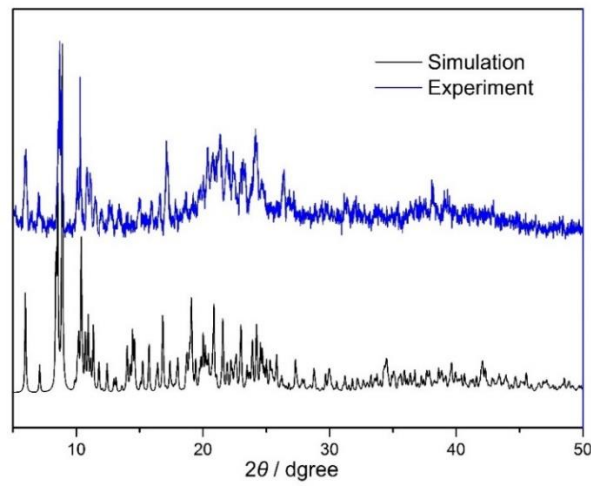


Fig. S7 X-ray powder diffraction pattern of complex **7_{Gd}**.

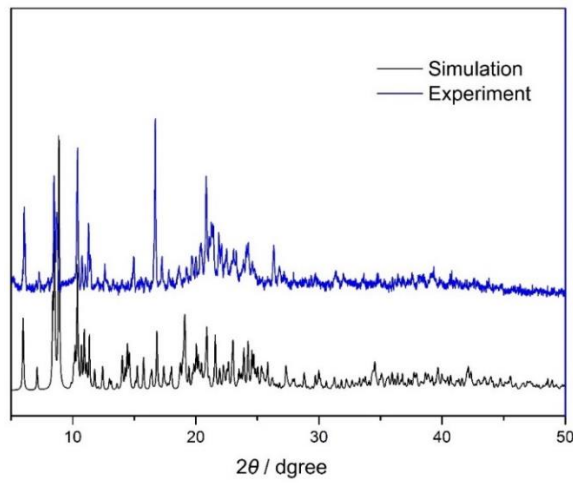


Fig. S8 X-ray powder diffraction pattern of complex **8_{Tb}**.

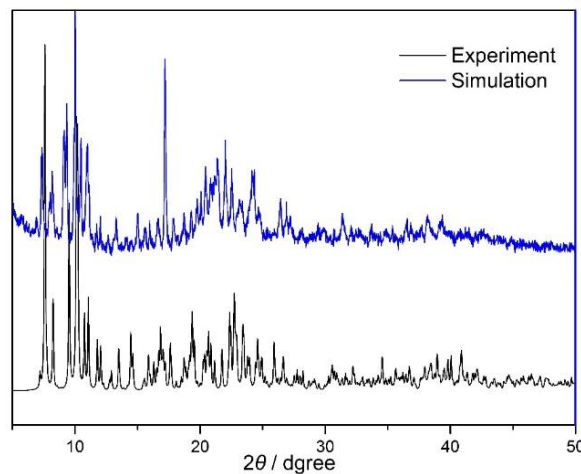


Fig. S9 X-ray powder diffraction pattern of complex **9_{Dy}**.

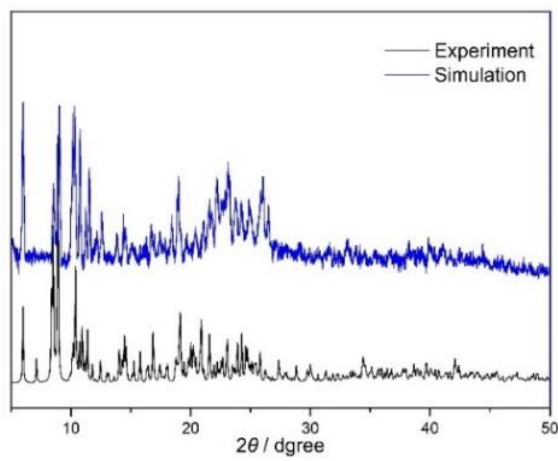


Fig. S10 X-ray powder diffraction pattern of complex **10_{Ho}**.

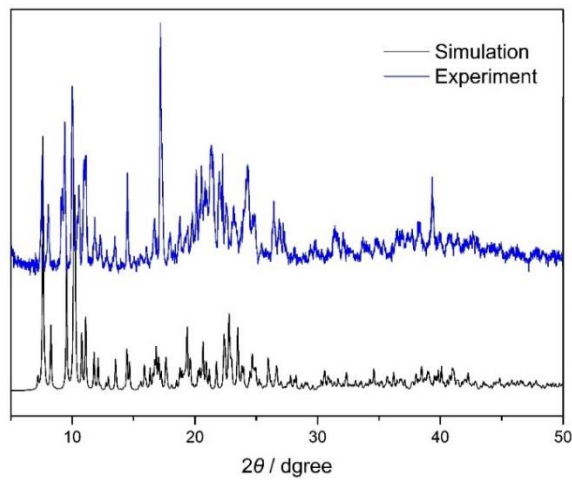


Fig. S11 X-ray powder diffraction pattern of complex **11_{Er}**.

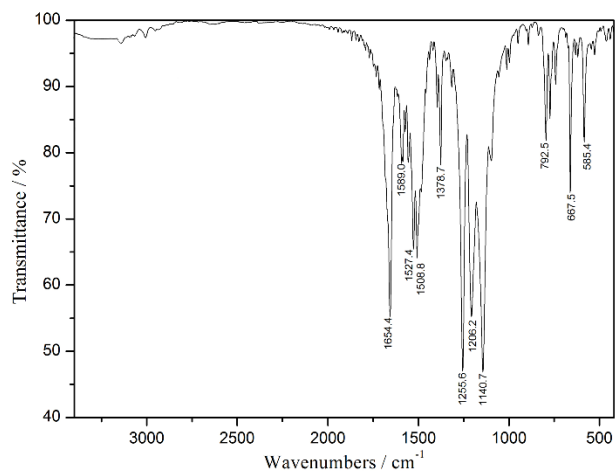


Fig. S12 Infrared spectrum of complex **1_{Gd}** at room temperature.

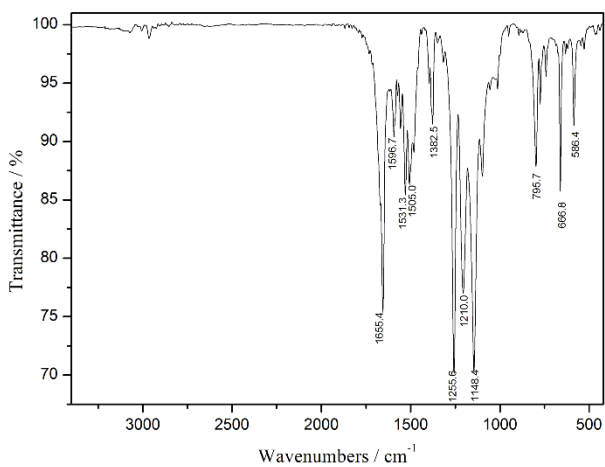


Fig. S13 Infrared spectrum of complex **2T_b** at room temperature.

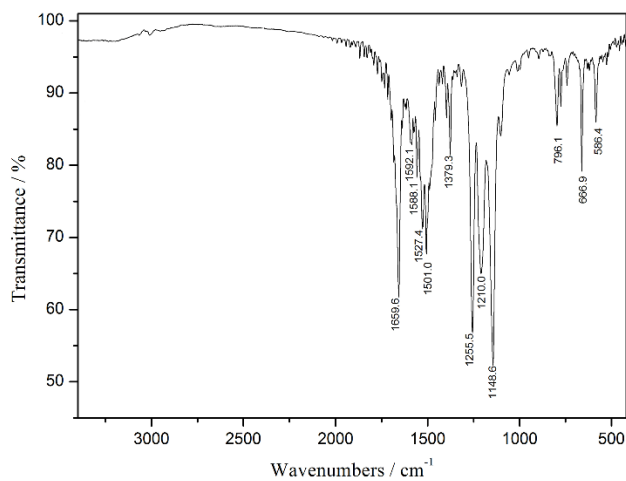


Fig. S14 Infrared spectrum of complex **3D_y** at room temperature.

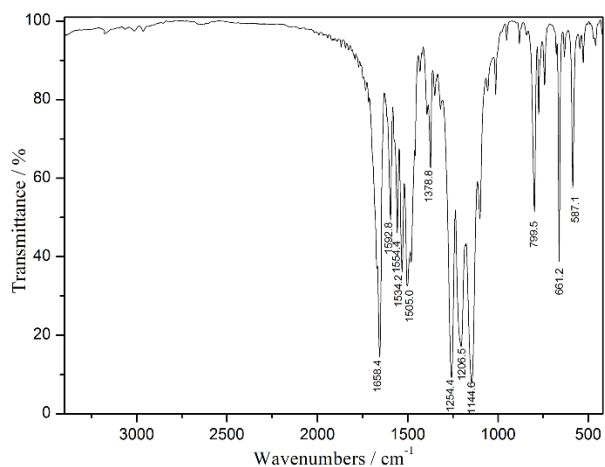


Fig. S15 Infrared spectrum of complex **4H_o** at room temperature.

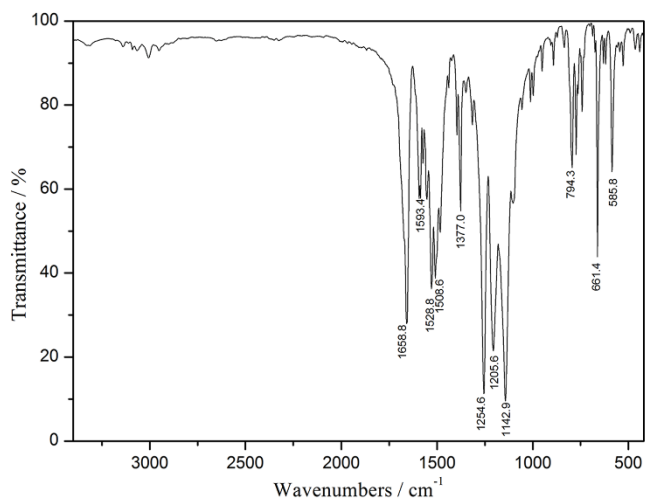


Fig. S16 Infrared spectrum of complex **5_{Er}** at room temperature.

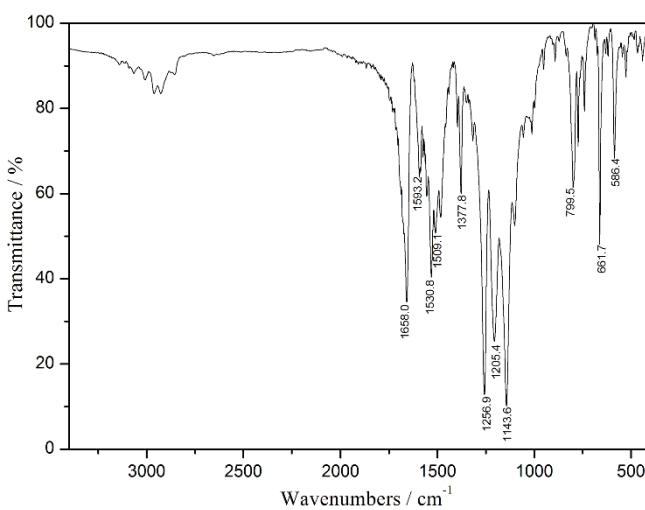


Fig. S17 Infrared spectrum of complex **6_{Yb}** at room temperature.

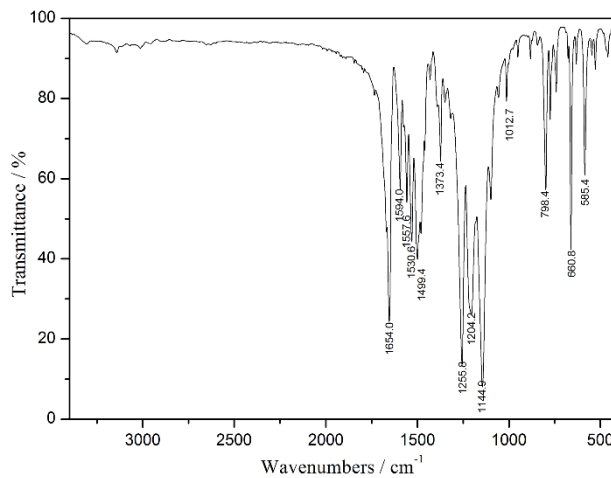


Fig. S18 Infrared spectrum of complex **7_{Gd}** at room temperature.

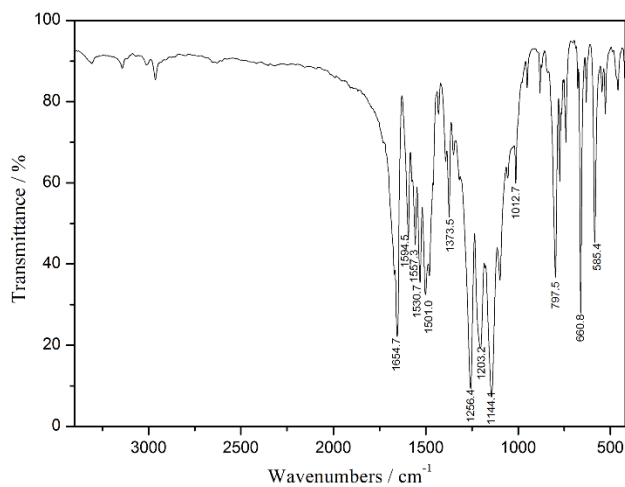


Fig. S19 Infrared spectrum of complex **8T_b** at room temperature.

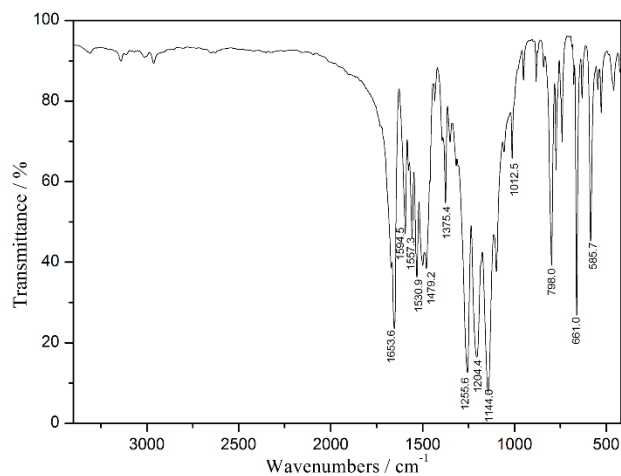


Fig. S20 Infrared spectrum of complex **9D_y** at room temperature.

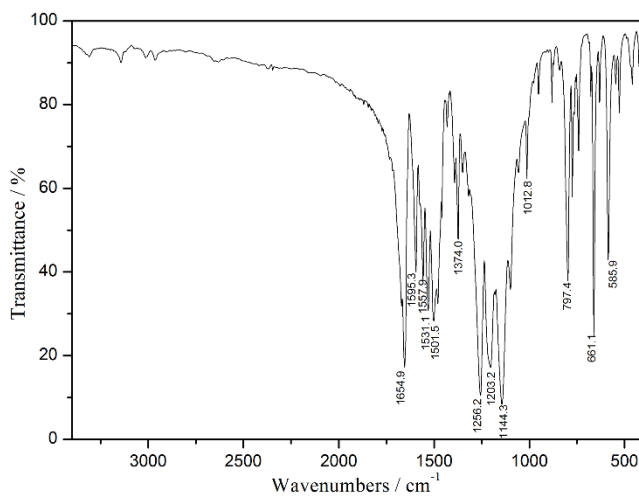


Fig. S21 Infrared spectrum of complex **10H_o** at room temperature.

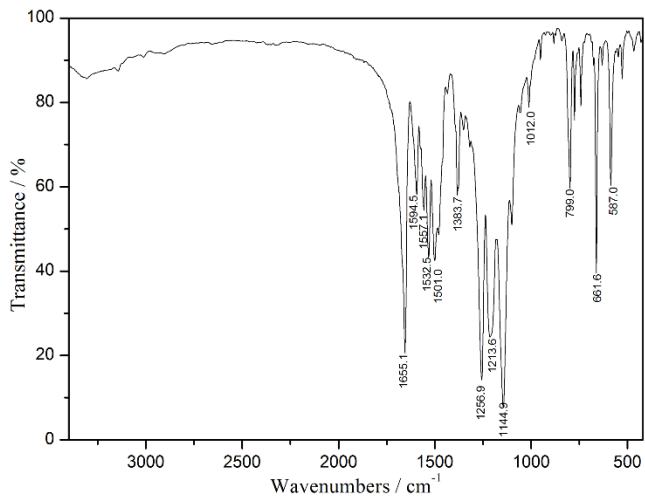


Fig. S22 Infrared spectrum of complex **11_{Er}** at room temperature.

2. Magnetic Properties

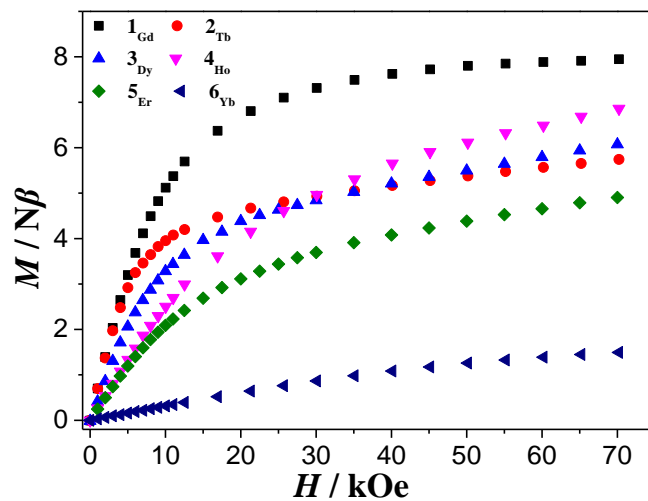


Fig. S23 Field dependent magnetizations at 2 K for **1_{Gd}-6_{Yb}**.

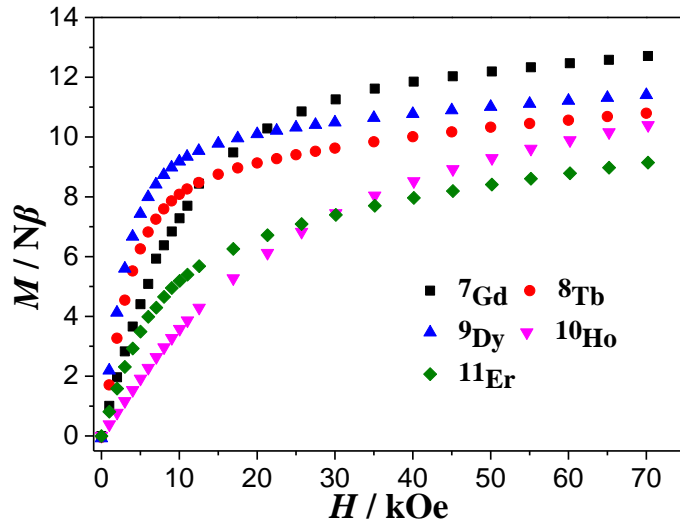


Fig. S24 Field dependent magnetizations at 2 K for **7Gd-11Er**.

Table S14. Relaxation fitting parameters from the least-square fitting of the Cole-Cole plots of **6Yb** according to the generalized Debye model.

Temperature / K	$\chi_s / \text{cm}^3\text{mol}^{-1}\text{K}$	$\chi_T / \text{cm}^3\text{mol}^{-1}\text{K}$	τ / s	α
1.8	8.69	13.94	0.0010	0.0058
2.0	8.50	13.65	0.0009	0.0036
2.4	8.69	13.33	0.0008	0.0032
2.6	8.69	12.83	0.0007	0.0027
2.8	8.49	12.18	0.0006	0.0025
3.0	8.47	11.41	0.00048	0.0015
3.2	8.46	10.75	0.00038	0.0020

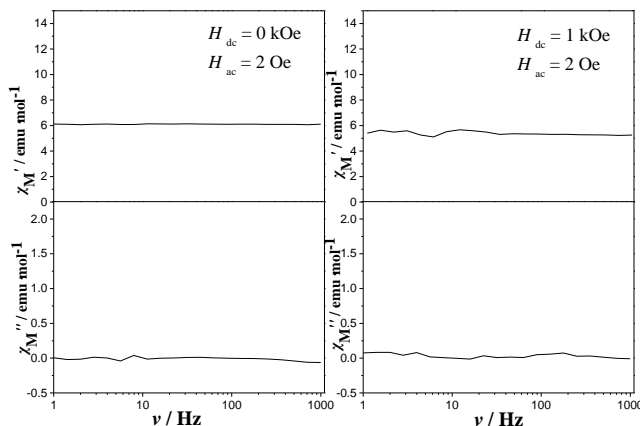


Fig. S25 The real and imaginary components of ac magnetic susceptibility for **2Tb** at 2 K under zero applied external dc field (left) and a dc field of 1000 Oe (right).

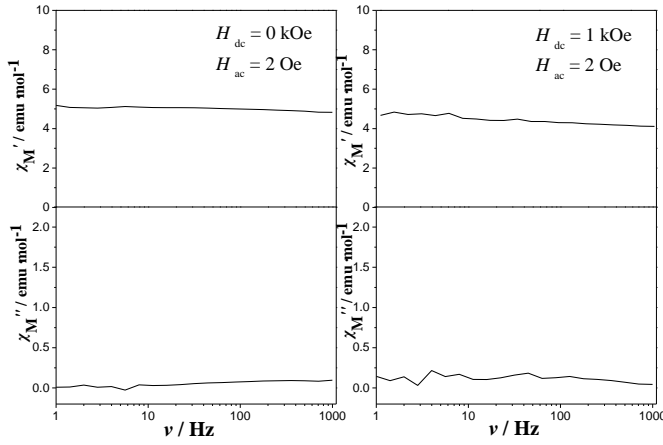


Fig. S26 The real and imaginary components of ac magnetic susceptibility for $\mathbf{3}_{\text{Dy}}$ at 2 K under zero applied external dc field (left) and a dc field of 1000 Oe (right).

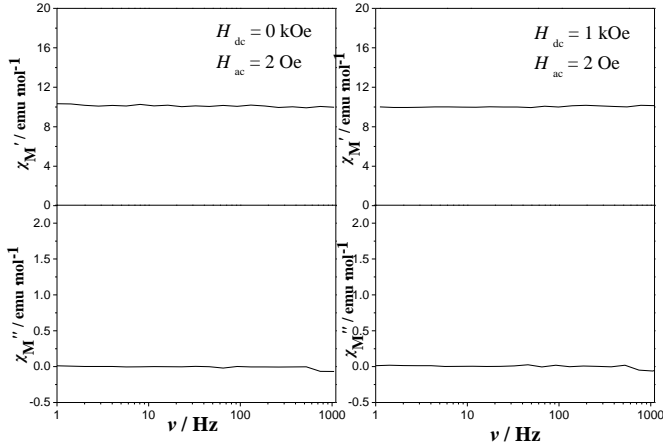


Fig. S27 The real and imaginary components of ac magnetic susceptibility for $\mathbf{4}_{\text{Ho}}$ at 2 K under zero applied external dc field (left) and a dc field of 1000 Oe (right).

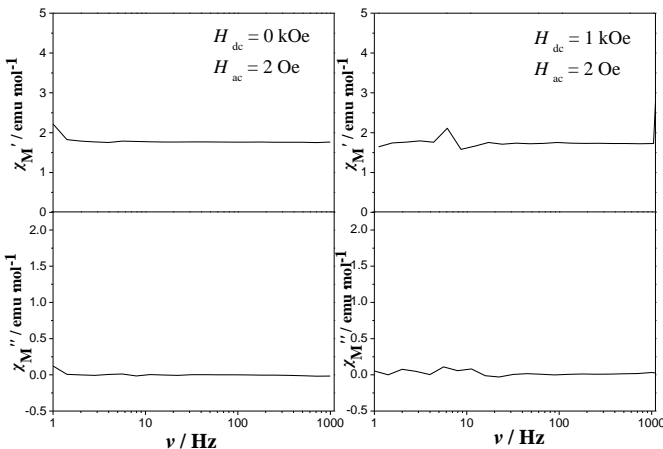


Fig. S28 The real and imaginary components of ac magnetic susceptibility for $\mathbf{5}_{\text{Er}}$ at 2 K under zero applied external dc field (left) and a dc field of 1000 Oe (right).

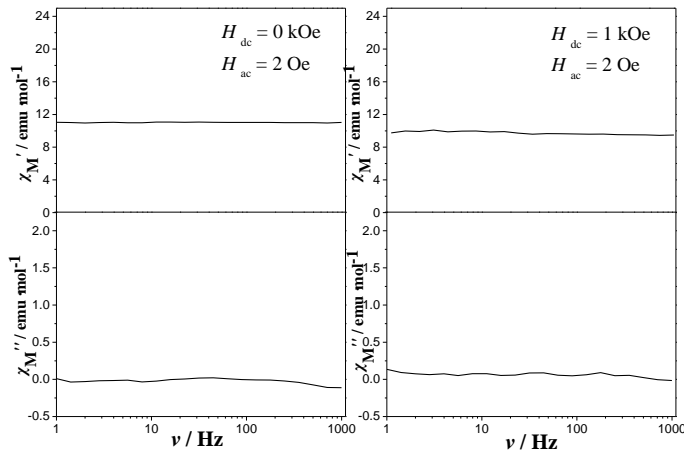


Fig. S29 The real and imaginary components of ac magnetic susceptibility for **8Tb** at 2 K under zero applied external dc field (left) and a dc field of 1000 Oe (right).

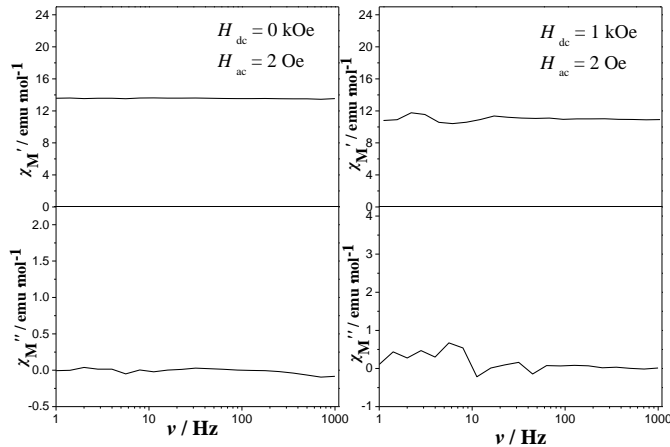


Fig. S30 The real and imaginary components of ac magnetic susceptibility for **9Dy** at 2 K under zero applied external dc field (left) and a dc field of 1000 Oe (right).

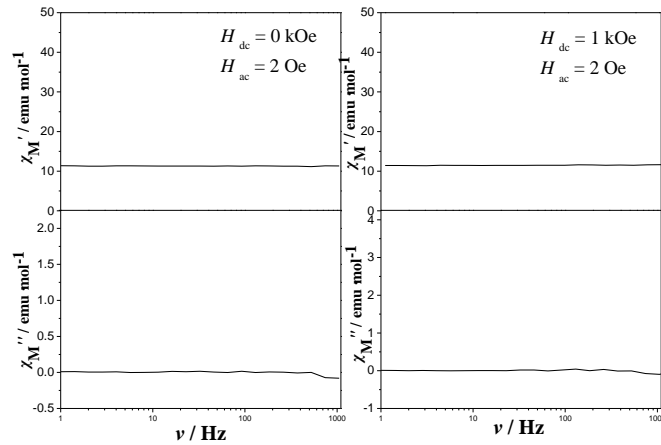


Fig. S31 The real and imaginary components of ac magnetic susceptibility for **10Ho** at 2 K under zero applied external dc field (left) and a dc field of 1000 Oe (right).

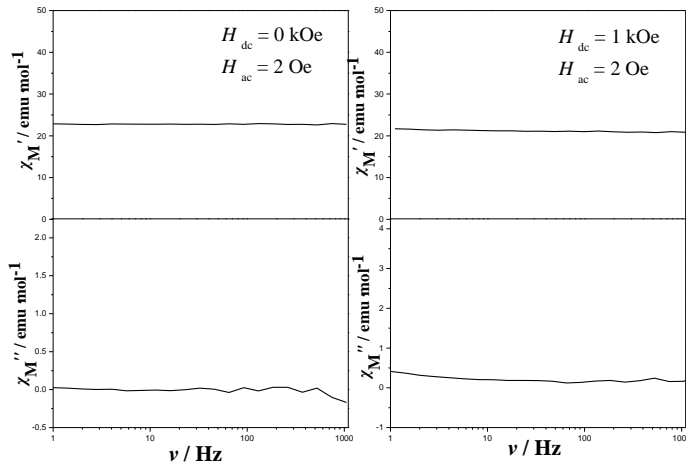


Fig. S32 The real and imaginary components of ac magnetic susceptibility for **11_{Er}** at 2 K under zero applied external dc field (left) and a dc field of 1000 Oe (right)

3. Details for calculations

Each of binuclear complexes **8_{Tb}–11_{Er}** has two types of individual Ln^{III} (lanthanide) fragments, and thus we calculated two types of individual Ln^{III} (Tb^{III}, Dy^{III}, Ho^{III} or Er^{III}) fragments for each of them. Complete-active-space self-consistent field (CASSCF) calculations on individual Ln^{III} (Tb^{III}, Dy^{III}, Ho^{III}, Er^{III} or Yb^{III}) fragment (see Fig. S22 for the calculated complete structure of individual Ln^{III} fragment) of complexes **2_{Tb}–6_{Yb}** and **8_{Tb}–11_{Er}** on the basis of single-crystal X-ray determined geometry have been carried out with MOLCAS 8.2^{S1} program package. During the calculations, individual Ln^{III} fragment was calculated keeping the experimentally determined structure of the corresponding compound while replacing the neighboring Ln^{III} ion by diamagnetic Lu^{III} for binuclear complexes **2_{Tb}–6_{Yb}** and **8_{Tb}–11_{Er}**, and the spin of the central radical was considered as 0.

The basis sets for all atoms are atomic natural orbitals from the MOLCAS ANO-RCC library: ANO-RCC-VTZP for Ln^{III} ion; VTZ for close O and N; VDZ for distant atoms. The calculations employed the second order Douglas-Kroll-Hess Hamiltonian, where scalar relativistic contractions were taken into account in the basis set and the spin-orbit couplings were handled separately in the restricted active space state interaction (RASSI-SO) procedure. Active electrons in 7 active spaces include all *f*

electrons (CAS (8 in 7 for Tb^{III} ; 9 in 7 for Dy^{III} ; 10 in 7 for Ho^{III} ; 11 in 7 for Er^{III} ; 13 in 7 for Yb^{III}) in the CASSCF calculation. To exclude all the doubts, we calculated all the roots in the active space. We have mixed the maximum number of spin-free state which was possible with our hardware (all from 140 quintuplets and 68 from 500 triplets for Tb^{III} ; all from 21 sextets, 128 from 224 quadruplets and 130 from 490 doublets for individual Dy^{III} fragment; all from 35 septuplets, 150 from 210 triplets and 120 from 196 singlets for individual Ho^{III} fragment; all from 35 quadruplets and all from 112 doublets for individual Er^{III} fragment; all from 21 triplets; and all from 21 sextets, all from 7 doublets for individual Yb^{III} fragment). SINGLE_ANISO^{S2} program was used to obtain the \mathbf{g} tensors, energy levels, magnetic axes, *et al.*, based on the above CASSCF/RASSI-SO calculations.

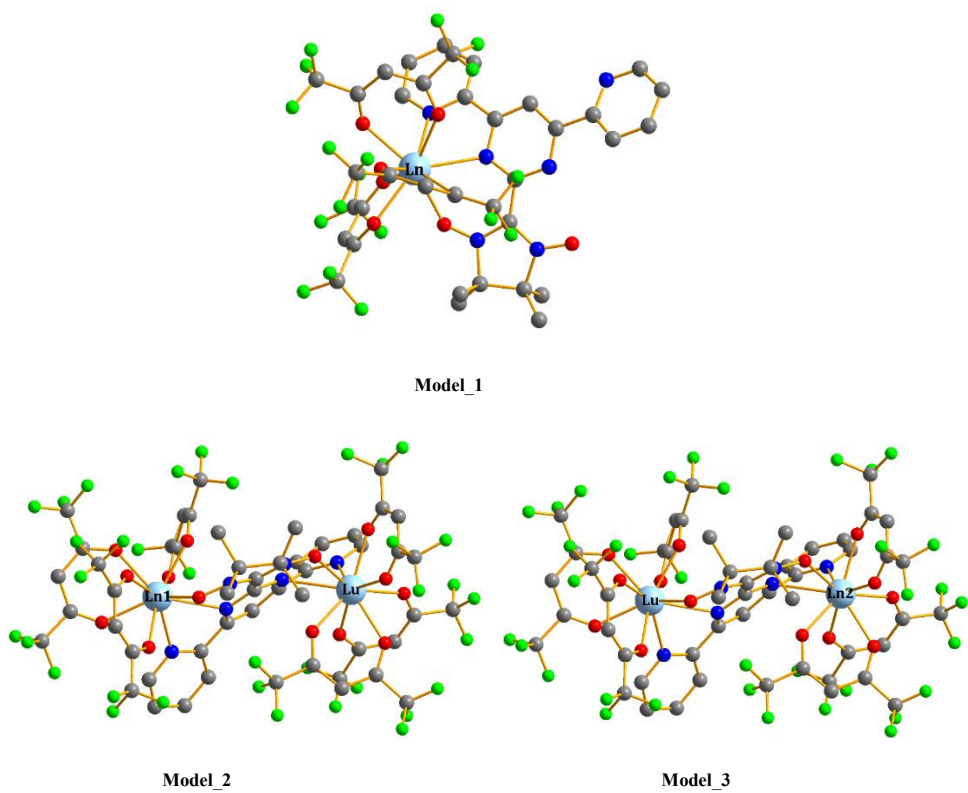


Fig. S33 Calculated model structures of individual Ln^{III} (Tb^{III} , Dy^{III} , Ho^{III} , Er^{III} or Yb^{III}) fragments; H atoms are omitted.

Table S15. Calculated energy levels (cm^{-1}), \mathbf{g} (g_x , g_y , g_z) tensors and m_J values of the lowest several spin-orbit states of individual Ln^{III} fragment (Tb^{III} , Dy^{III} , Ho^{III} , Er^{III} or Yb^{III}) for complexes **2_{Tb}–6_{Yb}** and **8_{Tb}–11_{Er}** using CASSCF/RASSI-SO with MOLCAS 8.2.

	2 _{Tb}			3 _{Dy}			4 _{Ho}		
	E/cm^{-1}	\mathbf{g}	m_J	E/cm^{-1}	\mathbf{g}	m_J	E/cm^{-1}	\mathbf{g}	m_J
1	0.0	0.000	± 6	0.0	0.773	$\pm 15/2$	0.0	0.000	± 8
	0.9	0.000 17.598			2.877 17.131		9.9	0.000 15.659	
	69.8	0.000		± 5	36.7		35.4	0.000	± 7
2	76.3	0.000 13.685			$\pm 13/2$	59.0	0.000 7.961		
	101.5	0.000	± 4	70.6		0.628	77.2	0.000	± 1
3	111.8	0.000 9.100			4.828 13.840	$\pm 7/2$	93.7	0.000 4.667	
	133.4				117.2		105.6		0
4	162.1	0.000	± 1	173.5	1.245 1.719	$\pm 1/2$	143.7	0.000	± 5
	170.8	0.000 12.201			2.086 13.248		166.8	0.000 10.566	
	225.5	0.000		± 2	198.8	$\pm 3/2$	175.6	0.000	± 6
6	227.7	0.000 14.606			0.431 1.447 13.902		184.9	0.000 12.156	
	356.5	0.000	± 3	226.0	0.414	$\pm 11/2$	191.4	0.000	± 2
7	356.7	0.000 17.572			2.910 14.711		235.0	0.000 5.780	
8				347.2	0.0472	$\pm 9/2$	258.7	0.000	± 4
					0.0679		278.5	0.000 11.999	
					19.3072				
9							306.8	0.000	± 3
							309.6	0.000 15.964	
	5 _{Er}			6 _{Yb}			8 _{Tb} (Tb1)		
	E/cm^{-1}	\mathbf{g}	m_J	E/cm^{-1}	\mathbf{g}	m_J	E/cm^{-1}	\mathbf{g}	m_J
	1	0.0	$\pm 15/2$	0.0	0.712	$\pm 7/2$	0.00	0.000	± 6
					1.337		0.08	0.000 17.812	
					5.683				
2	52.5	3.087 4.228 9.055	$\pm 11/2$	103.5	4.334	$\pm 3/2$	144.5	0.000	± 5
					2.694		147.8	0.000 14.573	
					0.982				

3	121.6	1.323	$\pm 9/2$	192.7	4.083	$\pm 5/2$	246.3	0.000 0.000 11.230	± 4
		2.412			2.866		260.0		
		9.052			0.113				
4	150.6	0.314	$\pm 7/2$	321.1	1.277	$\pm 1/2$	333.5		0
		1.666			2.073				
		11.507			6.696				
5	187.3	1.930	$\pm 3/2$				363.2	0.000 0.000 9.733	± 3
		4.254					384.9		
		8.488							
6	238.1	0.152	$\pm 13/2$				443.9	0.000 0.000 14.081	± 2
		2.601					447.7		
		10.573							
7	275.6	6.261	$\pm 5/2$				635.7	0.000 0.000 17.696	± 1
		5.330					636.0		
		2.891							
8	336.9	1.115	$\pm 1/2$						
		3.517							
		13.356							
	8_{Tb}(Tb2)			9_{Dy}(Dy1)			9_{Dy}(Dy2)		
	E/cm^{-1}	<i>g</i>	m_J	E/cm^{-1}	<i>g</i>	m_J	E/cm^{-1}	<i>g</i>	m_J
	1	0.0	0.000	± 6	0.0	0.051	0.0	0.014	$\pm 15/2$
		0.1	0.000 17.845			0.071 18.809		0.042 19.650	
	2	149.1	0.000	± 5	87.1	0.987	95.1	0.651	$\pm 13/2$
		150.0	0.000 14.693			1.623 15.856		1.195 16.252	
	3	233.2	0.000	± 4	115.0	0.091	146.2	2.526	$\pm 11/2$
		240.7	0.000 13.999			2.642 15.832		3.244 13.734	
	4	266.4	0.0000	± 3	146.9	1.928	202.3	9.543	$\pm 9/2$
		270.6	0.0000 10.337			3.789 12.261		5.963 1.659	
	5	316.8		0	191.9	2.934		1.086	$\pm 7/2$
						5.350 10.672	$\pm 1/2$	4.661 10.176	
	6	353.8	0.000	± 2	271.6	1.122	337.4	1.989	$\pm 5/2$
		371.5	0.000 14.057			1.802 15.144		2.754 13.787	
	7	487.1	0.000	± 1	346.9	0.204	409.2	1.989	$\pm 1/2$
		489.5	0.000 17.421			2.014 16.6534		2.754 13.787	
8					364.8	0.063 2.877 15.639	$\pm 7/2$	543.0	0.288 0.518 19.021

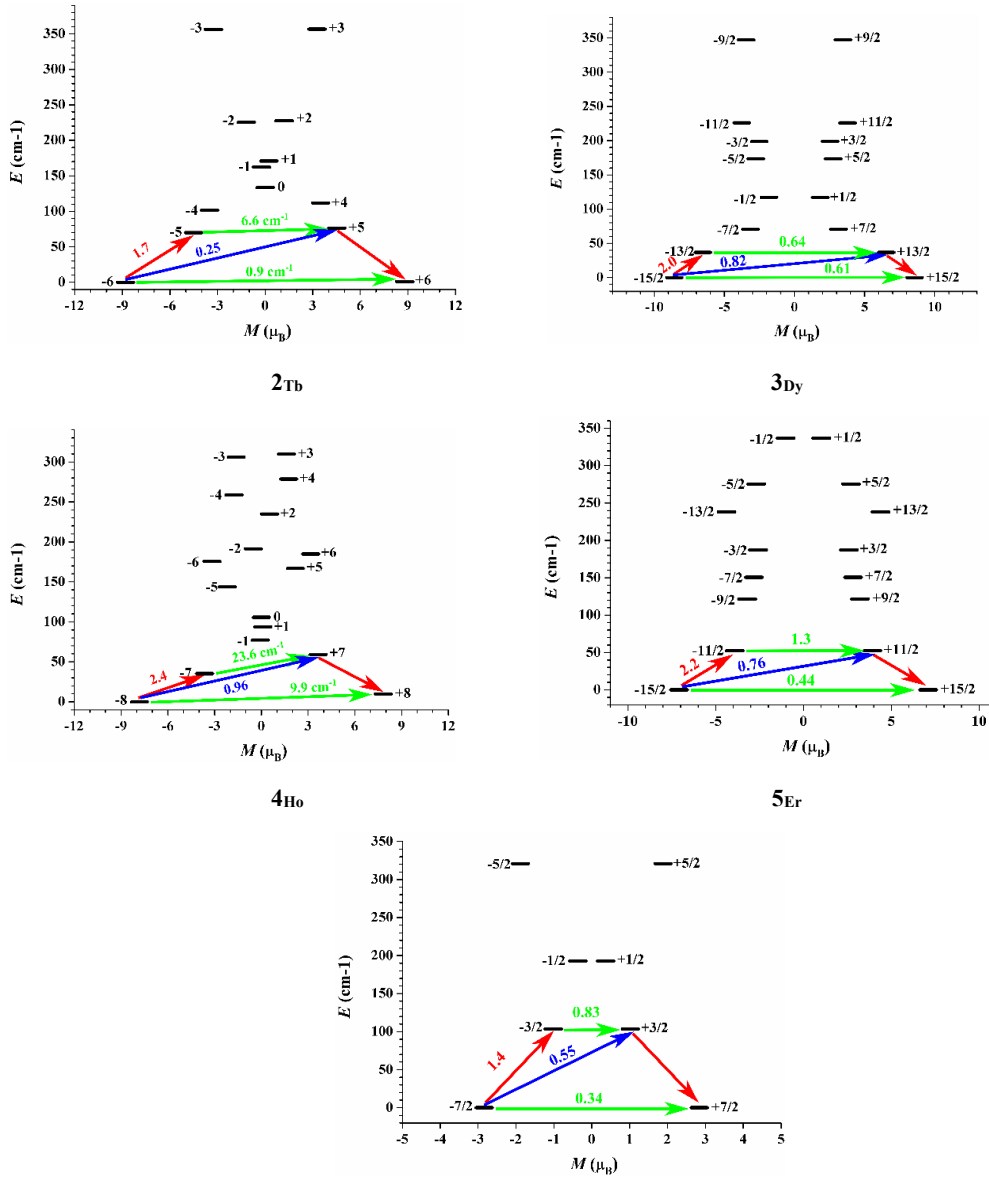
	10 _{Ho} (Ho1)			10 _{Ho} (Ho2)			11 _{Er} (Er1)		
	E/cm ⁻¹	g	<i>m_J</i>	E/cm ⁻¹	g	<i>m_J</i>	E/cm ⁻¹	g	<i>m_J</i>
1	0.0	0.000		0.0	0.000			1.731	
	6.9	0.000 17.687	± 8	4.8	0.000 18.596	± 8	0.0	4.312 12.732	$\pm 15/2$
2	58.5	0.000		66.4	0.000			7.952	
	69.5	0.000 13.943	± 5	70.8	0.000 15.280	± 3	48.2	4.682 0.828	$\pm 13/2$
3	103.1	0.000		102.7	0.000			1.108	
	109.8	0.000 12.497	± 7	120.1	0.000 12.808	± 6	106.0	1.574 12.425	$\pm 11/2$
4	145.4	0.000		132.5	0.000			0.221	
	173.8	0.000 12.848	± 3	166.3	0.000 9.408	± 4	140.0	4.196 8.734	$\pm 7/2$
5	207.0	0.000		195.6	0.000			0.735	
	212.8	0.000 14.345	± 4	202.7	0.000 10.841	± 5	176.1	2.103 10.950	$\pm 9/2$
6	234.6	0.000		224.2	0.000			7.095	
	256.3	0.000 12.400	± 1	231.5	0.000 10.532	± 2	211.3	4.778 1.075	$\pm 5/2$
7	289.2	0.000		272.4	0.000			2.559	
	306.6	0.000 8.738	± 6	279.4	0.000 7.784	± 7	275.2	3.440 10.408	$\pm 3/2$
8	334.1		0	298.3		0	342.6	0.434 1.716 15.417	$\pm 1/2$
9	352.0	0.000		331.6	0.000				
	362.4	0.000 14.933	± 2	339.1	0.000 16.153	± 1			
11 _{Er} (Er2)									
	E/cm ⁻¹	g	<i>m_J</i>						
1	0.0	0.815 1.591 14.787							
2	74.1	1.537 1.982 10.063	$\pm 11/2$						
3	117.7	0.512 2.846 11.165	$\pm 13/2$						
4	140.4	0.864 4.242 11.746	$\pm 9/2$						
5	173.7	1.464	$\pm 5/2$						

		2.412 5.653						
6	214.1	0.642	$\pm 3/2$					
		2.463						
		8.332						
7	265.9	2.665	$\pm 1/2$					
		4.859						
		8.392						
8	348.1	1.048	$\pm 7/2$					
		1.639						
		15.538						

Table S16. Wave functions with definite projection of the total moment $|m_J\rangle$ for the lowest two spin-orbit states of individual Ln^{III} fragments (Tb^{III} , Dy^{III} , Ho^{III} , Er^{III} or Yb^{III}) for complexes **2_{Tb}–6_{Yb}** and **8_{Tb}–11_{Er}** using CASSCF/RASSI-SO with MOLCAS 8.2.

	E/cm^{-1}	wave functions
2_{Tb}	0.0	95% $ \pm 6\rangle$
	0.9	
	69.8	
	76.3	
3_{Dy}	0.0	71% $ \pm 15/2\rangle$ +19% $ \pm 13/2\rangle$ +5% $ \pm 7/2\rangle$
	36.7	62% $ \pm 13/2\rangle$ +19% $ \pm 9/2\rangle$ +5% $ \pm 5/2\rangle$ +5% $ \pm 3/2\rangle$
4_{Ho}	0.0	41% $ \pm 8\rangle$ +16% $ \pm 7\rangle$ +23% $ \pm 6\rangle$ +6% $ \pm 3\rangle$ +9% $ \pm 2\rangle$
	9.9	
	35.4	
	59.0	
5_{Er}	0.0	50% $ \pm 15/2\rangle$ +29% $ \pm 11/2\rangle$ +14% $ \pm 7/2\rangle$
	52.5	17% $ \pm 13/2\rangle$ +31% $ \pm 11/2\rangle$ +9% $ \pm 7/2\rangle$ +26% $ \pm 5/2\rangle$ +6% $ \pm 3/2\rangle$ +5% $ \pm 1/2\rangle$
6_{Yb}	0.0	57% $ \pm 7/2\rangle$ +14% $ \pm 5/2\rangle$ +20% $ \pm 3/2\rangle$ +10% $ \pm 3/2\rangle$
	103.5	11% $ \pm 7/2\rangle$ +29% $ \pm 5/2\rangle$ +40% $ \pm 3/2\rangle$ +20% $ \pm 3/2\rangle$
8_{Tb} (Tb1)	0.00	98% $ \pm 6\rangle$
	0.08	
	144.5	
	147.8	
8_{Tb}(Tb2)	0.0	99% $ \pm 6\rangle$
	0.1	
	149.1	
	150.0	
9_{Dy}(Dy1)	0.0	81% $ \pm 15/2\rangle$ +13% $ \pm 11/2\rangle$
	87.1	50% $ \pm 13/2\rangle$ +20% $ \pm 9/2\rangle$ +18% $ \pm 7/2\rangle$
9_{Dy}(Dy2)	0.0	96% $ \pm 15/2\rangle$
	95.1	90% $ \pm 13/2\rangle$

10_{Ho(Ho1)}	0.0	66% ±8>+4% ±7>+17% ±6>+5% ±5>+5% ±4>
	6..9	
	58.5	
	69.5	17% ±7>+29% ±5>+8% ±4>+13% ±3>+6% ±2>+20% ±1>
10_{Ho(Ho2)}	0.0	85% ±8>+5% ±1>+6% ±0>
	4.8	
	66.4	5% ±7>+5% ±5>+28% ±4>+32% ±3>+17% ±2>
	70.8	
11_{Er(Er1)}	0.0	32% ±15/2>+27% ±13/2>+14% ±11/2>+11% ±9/2>+11% ±5/2>
	48.2	9% ±15/2>+26% ±13/2>+9% ±11/2>+19% ±9/2>+21% ±7/2>+12% ±3/2>
11_{Er(Er2)}	0.0	62% ±15/2>+21% ±13/2>+8% ±11/2>
	74.1	15% ±15/2>+6% ±13/2>+27% ±11/2>+11% ±9/2>+14% ±3/2>+24% ±1/2>



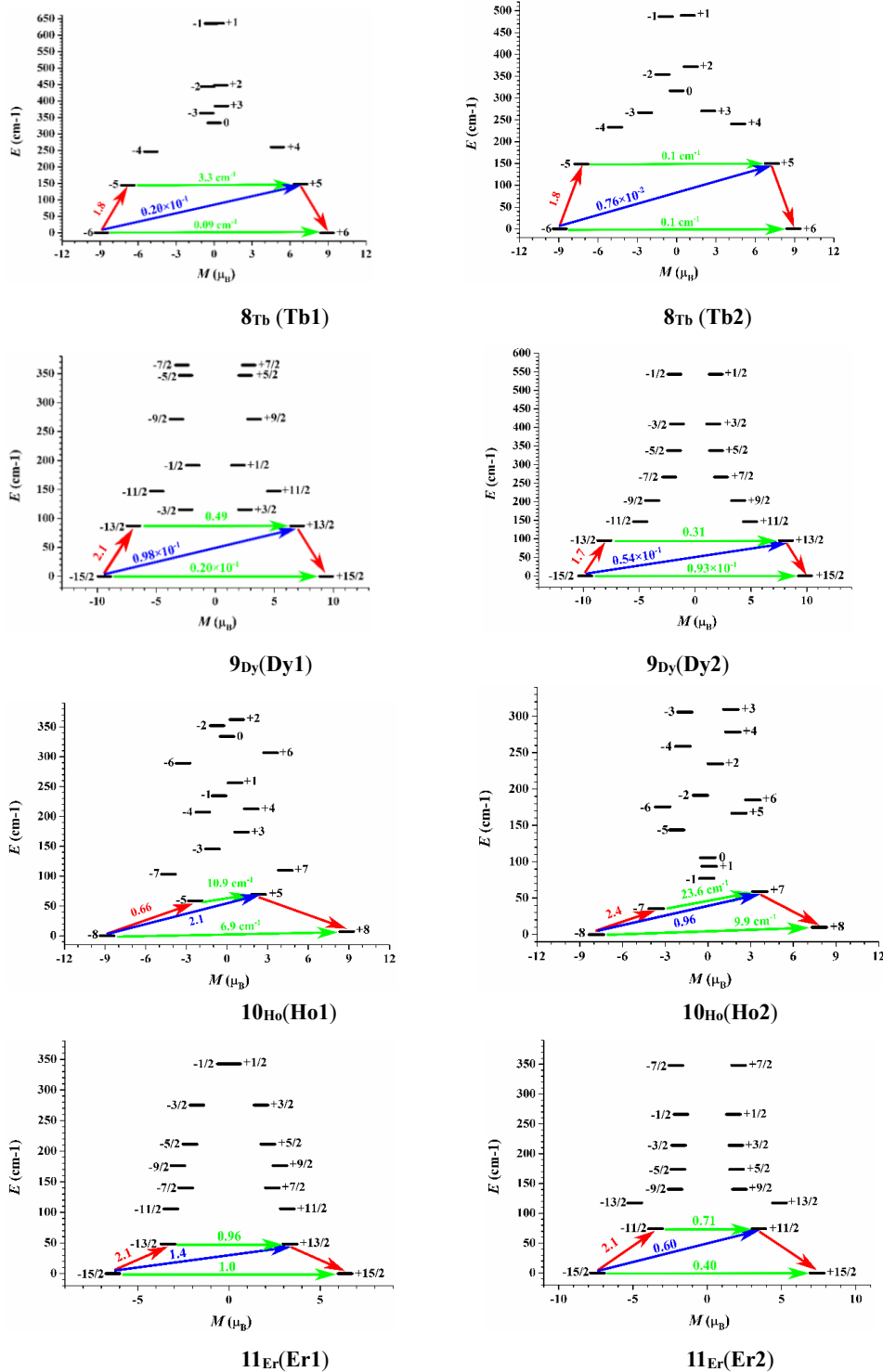


Fig. S34 Magnetization blocking barriers for individual Ln^{III} fragments in **2Tb–6Yb** and **8Tb–11Er**. The thick black lines represent the spin-orbit states as a function of their magnetic moment along the magnetic axis. The green lines correspond to the diagonal matrix element of the transversal magnetic moment; the blue lines represent Orbach relaxation processes. The path shown by the red arrows represents the most probable path for magnetic relaxation in the corresponding compounds. The numbers at each arrow stand for the mean absolute value of the corresponding matrix element of transition magnetic moment.

To fit the exchange interaction in complexes **1_{Gd}–11_{Er}**, we calculated individual Ln^{III} fragments using CASSCF to obtain the corresponding magnetic properties. Then, the exchange interaction between the magnetic centers is considered within the Lines model.^{S3} The Lines model is effective and has been successfully used widely in the research field of *f*-element single-molecule magnets.^{S4}

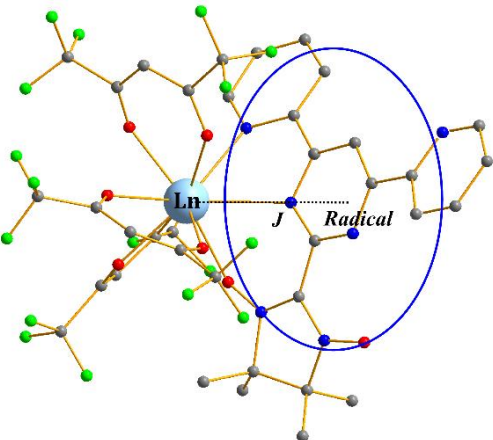


Fig. S35 Labeled one type of J in complexes **1_{Gd}–6_{Vb}**.

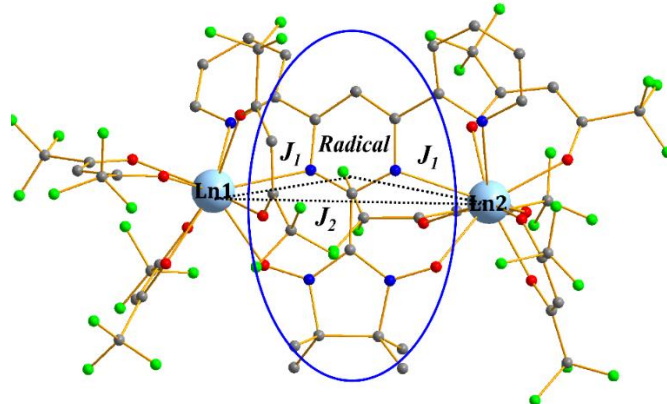


Fig. S36 Labeled two types of J in complexes **7_{Gd}–11_{Er}**.

For complexes **1_{Gd}–6_{Vb}**, there is only one type of J (see Fig. S24).

The exchange Ising Hamiltonian is:

$$\hat{H}_{exch} = -2J \hat{\tilde{S}}_{Ln} \hat{\tilde{S}}_{\text{Radical}} \quad (\text{S1})$$

For complexes **7_{Gd}–11_{Er}**, there are two types of J (see Fig. S25).

$$\hat{H}_{exch} = -2J_1 (\hat{\tilde{S}}_{Ln1} \hat{\tilde{S}}_{\text{Radical}} + \hat{\tilde{S}}_{Ln2} \hat{\tilde{S}}_{\text{Radical}}) - 2J_2 \hat{\tilde{S}}_{Ln1} \hat{\tilde{S}}_{Ln2} \quad (\text{S2})$$

The $\tilde{S}_{Ln} = \pm 1/2$ is the ground pseudospin on the Ln^{III} site, and the spin $S_{\text{Radical}} = 1/2$ is on radical site. The exchange coupling constants were fitted through comparison of the computed and measured magnetic susceptibilities using the POLY_ANISO program.^{S2}

Table S17. Exchange energies (cm⁻¹), energy difference between each exchange doublet Δ_{tun} (cm⁻¹) and main values of the g_z for the lowest several exchange doublets of complexes **2_{Tb}–6_{Yb}** and **8_{Tb}–11_{Er}**.

	2_{Tb}			3_{Dy}			4_{Ho}		
	E/cm^{-1}	$\Delta_{\text{tun}}/\mu\text{B}$	g_z	E/cm^{-1}	$\Delta_{\text{tun}}/\text{cm}^{-1}$	g_z	E/cm^{-1}	$\Delta_{\text{tun}}/\mu\text{B}$	g_z
1	0.0	0.19	14.803	0.0	1.9	15.363	0.0	0.60	4.435
2	3.1	0.20	18.798	10.7	1.7	18.621	10.0	0.70	0.389
	5_{Er}			6_{Yb}			8_{Tb}		
	E/cm^{-1}	$\Delta_{\text{tun}}/\text{cm}^{-1}$	g_z	E/cm^{-1}	$\Delta_{\text{tun}}/\text{cm}^{-1}$	g_z	E/cm^{-1}	$\Delta_{\text{tun}}/\mu\text{B}$	g_z
1	0.0	1.0	12.245	0.0	0.4	3.694	0.0	0.54×10^{-1}	29.422
2	5.1	0.3	16.094	1.2	0.1	7.672	0.4	0.40×10^1	24.066
3							4.1	0.33×10^1	20.111
4							4.6	0.32×10^{-1}	25.506
	9_{Dy}			10_{Ho}			11_{Er}		
	E/cm^{-1}	$\Delta_{\text{tun}}/\mu\text{B}$	g_z	E/cm^{-1}	$\Delta_{\text{tun}}/\mu\text{B}$	g_z	E/cm^{-1}	$\Delta_{\text{tun}}/\mu\text{B}$	g_z
1	0.0	0.22×10^{-1}	25.823	0.0	1.0	12.253	0.0	1.1	15.574
2	1.0	0.47	24.971	5.8	1.4	0.992	2.2	0.8	9.785
3	50.5	0.26	28.088	9.7	1.7	1.039	8.6	0.7	13.274
4	51.7	0.15×10^{-1}	28.978	15.6	1.5	15.707	9.9	0.7	18.433

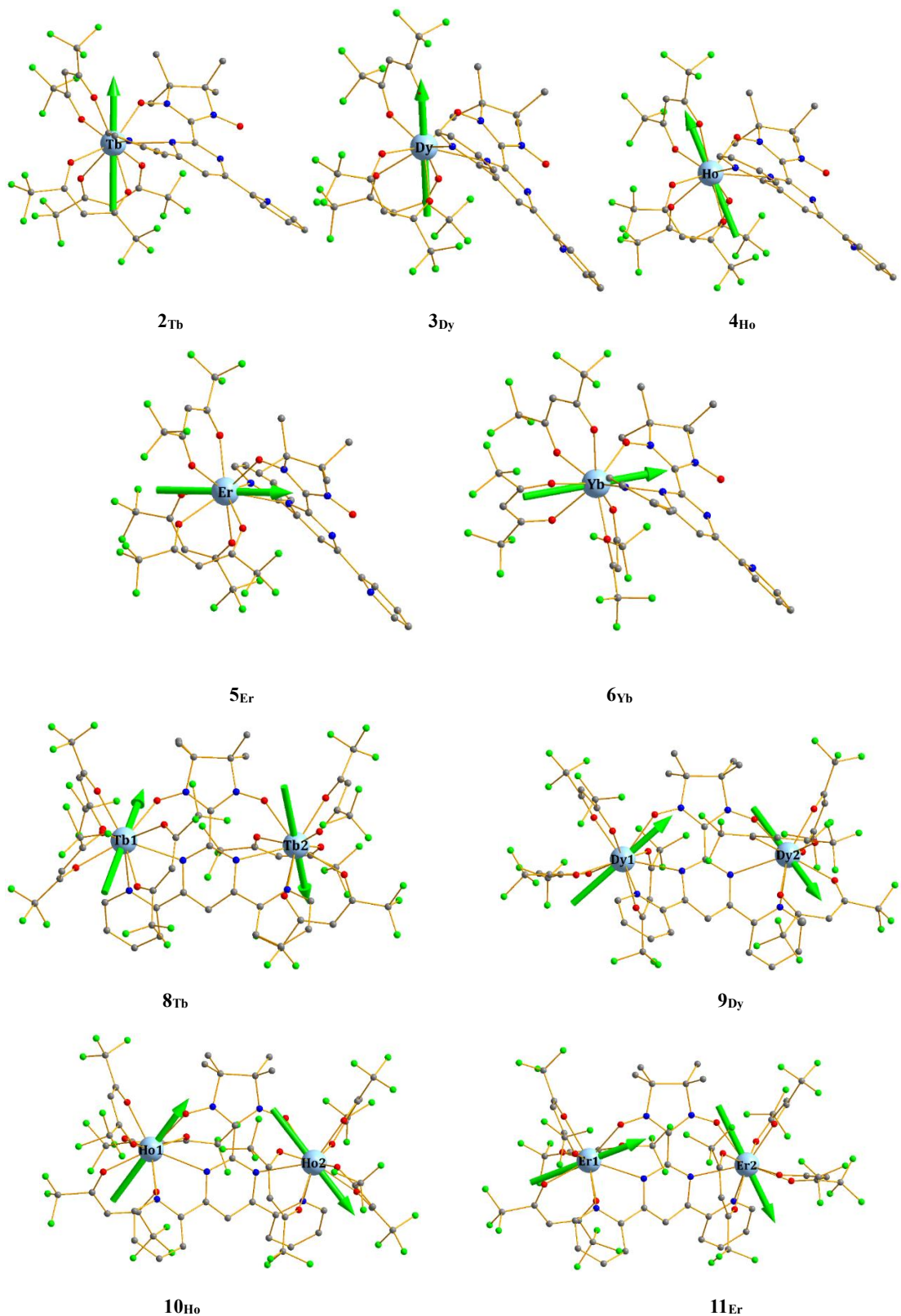


Fig. S37 Calculated orientations of the local main magnetic axes of the ground spin-orbit state on Ln^{III} (Tb^{III} , Dy^{III} , Ho^{III} , Er^{III} or Yb^{III}) ions of complexes $\mathbf{2}_{\text{Tb}}\text{--}\mathbf{6}_{\text{Yb}}$ and $\mathbf{8}_{\text{Tb}}\text{--}\mathbf{11}_{\text{Er}}$.

4. Reference

- S1 F. Aquilante, J. Autschbach, R. K. Carlson, L. F. Chibotaru, M. G. Delcey, L. De Vico, I. Fdez. Galván, N. Ferré, L. M. Frutos, L. Gagliardi, M. Garavelli, A. Giussani, C. E. Hoyer, G. Li Manni, H. Lischka, D. Ma, P. Å. Malmqvist, T. Müller, A. Nenov, M. Olivucci, T. B. Pedersen, D. Peng, F. Plasser, B. Pritchard, M. Reiher, I. Rivalta, I. Schapiro, J. Segarra-Martí, M. Stenrup, D. G. Truhlar, L. Ungur, A. Valentini, S. Vancoillie, V. Veryazov, V. P. Vysotskiy, O. Weingart, F. Zapata, R. Lindh, *J. Comput. Chem.*, 2016, **37**, 506.
- S2 (a) L. F. Chibotaru, L. Ungur and A. Soncini, *Angew. Chem. Int. Ed.*, 2008, **47**, 4126; (b) L. Ungur, W. Van den Heuvel and L. F. Chibotaru, *New J. Chem.*, 2009, **33**, 1224; (c) L. F. Chibotaru, L. Ungur, C. Aronica, H. Elmoll, G. Pilet and D. Luneau, *J. Am. Chem. Soc.*, 2008, **130**, 12445.
- S3 M. E. Lines, *J. Chem. Phys.* 1971, **55**, 2977.
- S4 (a) K. C. Mondal, A. Sundt, Y. H. Lan, G. E. Kostakis, O. Waldmann, L. Ungur, L. F. Chibotaru, C. E. Anson and A. K. Powell, *Angew. Chem. Int. Ed.* 2012, **51**, 7550; (b) S. K. Langley, D. P. Wielechowski, V. Vieru, N. F. Chilton, B. Moubaraki, B. F. Abrahams, L. F. Chibotaru and K. S. Murray, *Angew. Chem. Int. Ed.* 2013, **52**, 12014.